FEASIBILITY OF THE NAVIER-STOKES HARMONIC BALANCE METHOD FOR MODELLING AIRCRAFT UNSTEADY AERODYNAMICS

Jernej Drofelnik[*] , **Andrea Da Ronch**[*] , **M. Sergio Campobasso**[**]
[*]**University of Southampton, Faculty of Engineering and the Environment. Southampton SO17 1BJ, United Kingdom. ,** [**]**University of Lancaster, Department of Engineering. Lancaster LA1 4YW, United Kingdom.**

Keywords: *aircraft flight dynamics; aerodynamic derivatives; Harmonic Balance Navier–Stokes equations; NASA Common Research Model; unsteady aerodynamics*

Abstract

Traditionally, the models of the unsteady aerodynamic loads needed for aircraft flight simulations have been estimated using the aerodynamic derivatives approach, which, using linear aerodynamic models, provides the influence of the aircraft motion rates on the aerodynamic forces and moments. With increasing aircraft maneuverability resulting in nonlinear unsteady flow regimes, however, the linearity assumption of the conventional aerodynamic derivatives approach makes the method questionable. Methods with higher reliability have been show to be achievable by using knowledge of the aircraft aerodynamic response to harmonic excitations. Prompted by the need of rapidly and accurately estimating such response, this study demonstrates the applicability of the nonlinear frequency–domain Navier–Stokes Harmonic Balance method for predicting periodic aircraft flows with low and high levels of nonlinearity. Using the NASA Common Research Model aircraft case study, it is found that the Harmonic Balance technology yields estimates of the unsteady forces differing negligibly from those of the standard time–domain Navier–Stokes method with a runtime analysis reduced by at least one order of magnitude over that of the time–domain approach.

1 Introduction

Aircraft flight simulation plays a key role in civil and military aviation. Flight simulators cover a full range of applications. The simulator serves as a basis of engineering design [1], and is used for discovering the flight characteristics of a new aircraft and increasing confidence in predicting aircraft performance and behavior prior to expensive flight testing. For these reasons, an accurate model of the aerodynamic loads is needed for aircraft flight simulation. Traditionally, the aerodynamic loads have been generated using the aerodynamic derivatives approach introduced by Bryan [2]. The approach relies on the principle of superposition to calculate the aerodynamic loads for a generic motion of the aircraft, and assumes that aerodynamic derivatives are invariant with flight parameters. Due to increased aircraft maneuverability into nonlinear flow regimes, the aerodynamic derivatives approach loses its validity. At present, there is no consensus on what is the best suited aerodynamic model for rapid aerodynamic predictions of nonlinear unsteady flows. Reynolds–averaged Navier–Stokes (RANS) Computational fluid dynamics (CFD) can predict nonlinear flow physics and has been successfully used to provide accurate aerodynamic data to determine aerodynamic derivatives [3]. However, the runtime of time–

domain (*TD*) RANS analyses is high even for two–dimensional (2D) problems, let apart a complete aircraft. *TD* RANS simulation of periodic flows require long runtimes as several oscillation cycles need to be simulated before achieving the sought periodic state. By solving the unsteady equations in the frequency–domain (*FD*), analysis runtimes can be significantly reduced. A popular *FD* method is the harmonic balance (*HB*) RANS technology, first introduced for turbomachinery blade aeroelasticity [4], and was later successfully applied to aircraft unsteady aerodynamics and aeroelasticity [3, 5, 6, 7, 8]. Use of the *HB* RANS method for these applications has been shown to reduce RANS analysis runtimes by one to two orders of magnitude with respect to conventional *TD* RANS analyses. Several other nonlinear *FD* NS methods exist and have been applied in the areas above, as discussed in [9].

In many challenging flow conditions, the *HB* method achieves good prediction accuracy while reducing significantly analysis runtimes over the *TD* method. However, the *HB* method may not be more convenient than the *TD* method when the periodic flow features high levels of stall [10]. Determining the range of operation in which it is computationally convenient to use the *HB* method is a challenging task. In this respect, this paper aims at investigating the use of the *HB* method to predict unsteady flows past the NASA Common Research Model aircraft [11] for different levels od flow nonlinearity. The objectives of this work are to: *a)* assess prediction robustness and reliability of the three–dimensional (3D) *HB* RANS technology for flight simulation; *b)* identify the flow conditions at which linearized *TD* or linear *FD* approaches fail; *c)* demonstrate that the *HB* method enables solving relatively complex flow problems while retaining a computational advantage; and *d)* assess the speedup achieved by the *HB* solver over its *TD* counterpart. To the best of the authors' knowledge, this study presents the application of the *HB* method on the largest grid reported in the open literature.

All reported simulations use the new in-house *HB* RANS solver COSA [12, 13], featuring Menter's shear stress transport (SST) model for the turbulence closure. The *TD* and *HB* RANS equations and the SST turbulence model are presented in Section 2, and a brief description of the numerical method is provided in Section 3. Section 4 describes the NASA Common Research Model test case, various steady and unsteady flow regimes of which are analyzed in Section 5; the study summary is provided in Section 6.

2 Governing equations

2.1 Time–domain equations

The 3D compressible Navier–Stokes equations are a system of conservation laws expressing the conservation of mass, momentum and energy of a viscous fluid flow. Averaging these equations on the turbulence time–scales yields the so–called RANS equations, which are formally similar to the NS equations but feature an additional term, the Reynolds stress tensor accounting in a mean fashion for the effects of turbulence. Making use of Boussinesq's approximation, this tensor is expressed as the product of an eddy viscosity and the strain rate tensor based on the mean velocity field. In the COSA CFD code used in this study, the former variable is computed with the two–equation $k - \omega$ SST turbulence model. Thus, turbulent compressible flows are determined by solving a system of $N_{pde} = 7$ partial differential equations (PDEs) and an equation of state linking fluid density, pressure and internal energy.

The Arbitrary Lagrangian–Eulerian (ALE) integral form of the system of the time–dependent RANS and SST equations is written in a Cartesian coordinate system. Given a control volume C with boundary S, the ALE integral form of the system of time–dependent RANS and SST equations is:

$$\frac{\partial}{\partial t} \left(\int_C \mathbf{U} dC \right) + \oint_S (\mathbf{\Phi}_c - \mathbf{\Phi}_d) \cdot d\underline{S} - \int_C \mathbf{S} dC = 0 \tag{1}$$

where $\mathbf{U} = [\rho \quad \rho \underline{u}^T \quad \rho E \quad \rho k \quad \rho \omega]^T$ is the array of conservative variables, the superscript T denotes the transpose operator, and the symbols

ρ, $\underline{u}$, E, k and ω denote, respectively, density, absolute velocity vector, and total energy, turbulent kinetic energy and specific dissipation rate of turbulent kinetic energy per unit mass. The total energy is $E = e + (\underline{u} \cdot \underline{u})/2 + k$, where e denotes the internal energy per unit mass; the perfect gas law is used to express the static pressure p as a function of ρ, E, k and the mean flow kinetic energy per unit mass $(\underline{u} \cdot \underline{u})/2$. The definitions of the generalized convective flux vector $\underline{\Phi}_c$, the generalized diffusive flux vector $\underline{\Phi}_d$ and the source term $\mathbf{S}$ are reported in [14].

2.2 Harmonic balance equations

The derivation of the *HB* RANS and SST equations may be found in [4, 9]. For completeness, a qualitative description of the derivation is provided below. The sought periodic flow field is written as a truncated Fourier series with $(2N_H + 1)$ spatial position–dependent components, where N_H indicated the desired number of harmonics. The harmonic motion is executed at a fundamental frequency Ω. The Fourier series approximation of the solution is inserted in the *TD* governing equations expressed by Eq. (1). This operation results in the original system of N_{pde} time–dependent PDEs becoming a system of $[N_{pde} \times (2N_H + 1)]$ time–independent PDEs, the solution of which yields the $(2N_H + 1)$ components of the truncated Fourier series. However, writing the *HB* RANS and turbulence model equations in the Fourier space turns out to be challenging, due to the high level of nonlinearity of the equations involved; for this reason, Ref. [4] proposed to re–cast the *HB* CFD equations in the time–domain. Indeed, this choice simplifies substantially the construction of the *HB* equations and also the implementation of this technology in an existing CFD code. Formally, re–casting the *HB* equations in the time–domain results in the *HB* equations becoming a system of $(2N_H + 1)$ steady flow problems, and the *HB* solution becoming a set of equally spaced flow states or snapshots of the sought periodic flow. Once determined, the *HB* solution can be re–cast in the Fourier space by using a suitably defined Fourier

transformation operator.

Ultimately, one finds that the desired *HB* form of the conservation laws to be:

$$
\Omega D \left(\int_{C_H} \mathbf{U}_H \, dC_H \right) +
$$
$$
\oint_{S_H} (\underline{\Phi}_{cH} - \underline{\Phi}_{dH}) \cdot d\underline{S}_H - \int_{C_H} \mathbf{S}_H dC_H = 0 \quad (2)
$$

The unknown array $\mathbf{U}_H$ consists of $(2N_H + 1)$ periodic flow snapshots at $(2N_H + 1)$ equally spaced times t_n:

$$
t_n = \frac{n}{(2N_H + 1)} \frac{2\pi}{\Omega}, \qquad n = 0, 1, \ldots, 2N_H \quad (3)
$$

The structure of the array $\mathbf{U}_H$ is thus: $\mathbf{U}_H = [\tilde{\mathbf{U}}(t_0)^T \; \tilde{\mathbf{U}}(t_1)^T \ldots \tilde{\mathbf{U}}(t_{N_H})^T]^T$, and is the same of that of all other variables with a subscript H appearing in Eq. (2). The spectral operator D is a $[(2N_H + 1) \times (2N_H + 1)]$ antisymmetric matrix, defined in [9], which couples all $(2N_H + 1)$ flow snapshots. It can be shown that the entry (m, n) of D is:

$$
D_{mn} = \frac{2}{2N_H + 1} \sum_{k=1}^{N_H} k \sin \left(\frac{2\pi k(n - m)}{2N_H + 1} \right), \quad (4)
$$
$$
m, n = 0, 2N_H
$$

Moving from the conventional *TD* to the *HB* formulation of the governing equations, one has to solve $[N_{pde} \times (2N_H + 1)]$ time–independent or steady PDEs rather than N_{pde} time–dependent PDEs. The solution of each steady PDE requires substantially less computational work than that of a time–dependent PDE. This cost reduction outweighs the burden of solving more PDEs in the *HB* case and thus the overall computational cost of solving the *HB* equations turns out to be smaller than that required for solving the *TD* equations. Therefore, turbulent periodic flows can be computed significantly faster using the *HB* rather than the *TD* approach in many engineering applications. This is because of the avoidance of the physical transient leading to the periodic state.

3 Numerical solution

The finite volume cell–centered parallel RANS CFD COSA code solves both the *TD* RANS and SST equations [12, 14] and their *HB* counterparts [10] using structured multi–block grids. The discretization of the convective fluxes of both RANS and SST PDEs uses Van Leer's MUSCL extrapolations and Roe's flux–difference splitting with Van Albada's flux limiter. The discretization of the diffusive fluxes and the turbulent source terms uses central finite–differencing [14].

The integration of the steady and *HB* RANS and SST equations is performed in a fully–coupled fashion using explicit Runge–Kutta time–marching, with local time–stepping, implicit residual smoothing and multigrid for convergence acceleration. *TD* problems are solved using Jameson's second–order dual–time stepping.

Harten's entropy correction [15] is used to assure physically relevant solutions, when there is a presence of expansion shocks and contact discontinuities in the solutions.

Boundary conditons used in this study are as follows. At viscous wall boundaries, i.e. wing and fuselage, the no–slip condition is applied. In order to halve the computational cost, the symmetry boundary condition is used at the symmetry plane. On the far–field, the freestream boundary condition based on one–dimensional Riemann invariants was used.

4 Test case

The test case is for the transonic NASA Common Research Model (CRM) [11]. This test case was primarily developed for the purpose of CFD validation studies, therefore, it will first serve as a validation test case for COSA CFD code. Furthermore, it will be used to predict dynamic loads of periodic flows using the *TD* and *HB* RANS equations.

4.1 Common Research Model

NASA CRM consists of a contemporary transonic supercritical wing design, and was developed with well behaved aerodynamic characteristics. The fuselage is representative of a wide/body commercial transport aircraft and includes a wing–body fairing, as well as a scrubbing seal for the horizontal tail. In this study, only the body–wing configuration was used. The computational grids were adopted from the 5th AIAA CFD Drag Prediction Workshop [16]. A multi-block, O–O grid topology was provided for the wing–body configuration. Six grid levels were provided, however, to keep the computational cost within the size of the available resources, only four grid levels were used in this study: tiny (638,976 cells), coarse (2,156,544 cells), medium (5,111,808 cells) and fine (17,252,352 cells). A view of the surface mesh of the tiny grid is depicted in Fig. 1.
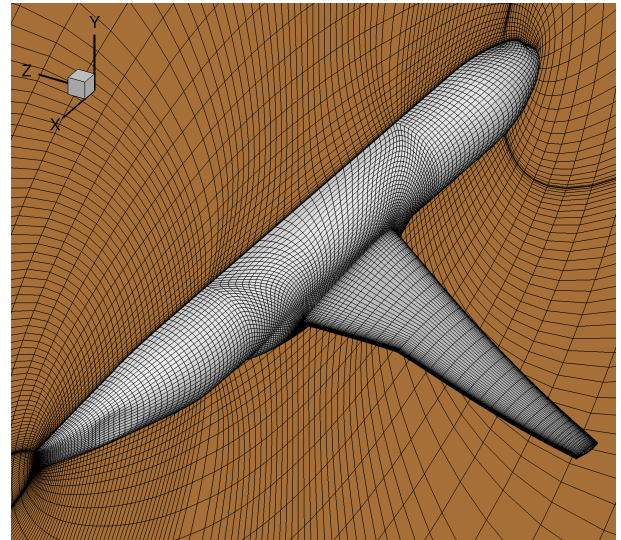

Fig. 1 Multi-block (tiny) grid of the NASA CRM.

Experimental measurements for the NASA CRM supercritical model, obtained from [17], were conducted at Mach number $M_\infty = 0.85$, freestream temperature $T_\infty = 311$ K, and Reynolds number $Re = 5.0$ million (based on reference chord $Cref = 275.80$ in) for various angles of attack. Experiments were conducted both at the National Transonic Facility and the NASA Ames 11 Foot Wind Tunnel. In this study, only the data from National Transonic Facility are used. Reference [18] reported that the initial comparisons between CFD and experimental

4

results from both wind tunnels were disappointing. This happened due to the effects of the swept–strut mounting system and the geometry of the wing used in the computational analysis. The problem was that the CRM wing geometry used for the Fifth Drag Prediction Workshops was defined prior to the building and testing of the CRM wind tunnel model, therefore, during the wind tunnel tests, the model deformed under the loading. In order to provide a measure for comparison, a correction to the experimental data from National Transonic Facility was proposed in [18].

5   Results

5.1   Validation

Polars were computed for the CRM wing–body configuration. Figure 2 shows the predicted lift coefficient C_l, the drag coefficient C_d and the pitching moment coefficient C_m for various values of angle of attack, at four different grid levels. There are significant differences among the four grid levels for all forces and moment coefficients, however, the computed lift curve of fine grid level is in excellent agreement with the corrected experimental data set. All forces and moment coefficients are well within the uncertainty bands of reported CFD results at the 5th AIAA CFD Drag Prediction Workshop [18]. Therefore, we are confident of the validity of our CFD solver.

5.2   Forced sinusoidal motion–case A

Case A is an unsteady flow problem executed below the first break point in the lift coefficient, which is found to occur at about 3 deg.

5.2.1   Numerical set–up

The forced sinusoidal motion is defined by $\alpha_\infty(t) = \alpha_0 + \alpha_A \sin(2k\tau)$. For Case A, the reduced frequency is $k = \frac{\omega c_{ref}}{2U_\infty} = 0.08$, where ω represent the oscillation frequency, c_{ref} is the reference chord, and U_∞ is the freestream velocity. The mean angle of attack is $\alpha_0 = 0$ deg and the amplitude is $\alpha_A = 3$ deg. The symbol $\tau = \frac{tU_\infty}{c_{ref}}$
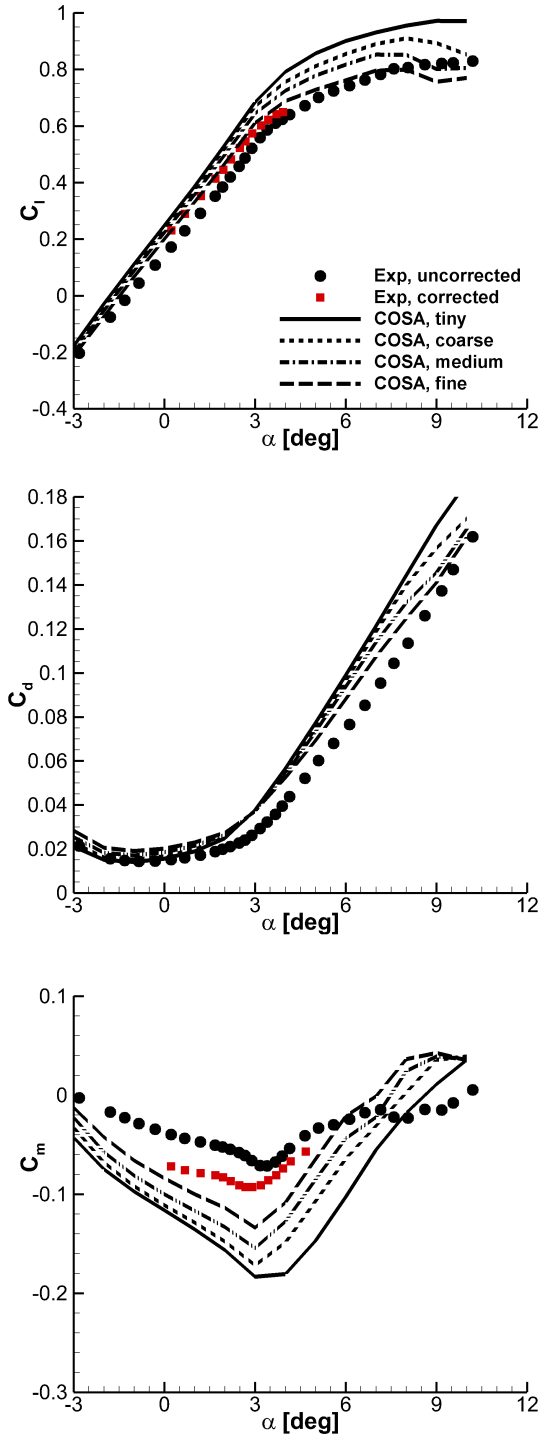
Fig. 2 Forces and moment coefficients of the NASA CRM ($M_\infty = 0.85$, $T_\infty = 311$ K, $Re = 5.0$ million).

is the non–dimensional time, where t represents the physical time. The flow field is characterized by the formation of a strong and highly dy-

namic shock wave. The motivation for such high reduced frequency comes from the experimental cases of forced motion, traditionally used to extract aerodynamic derivatives [3].
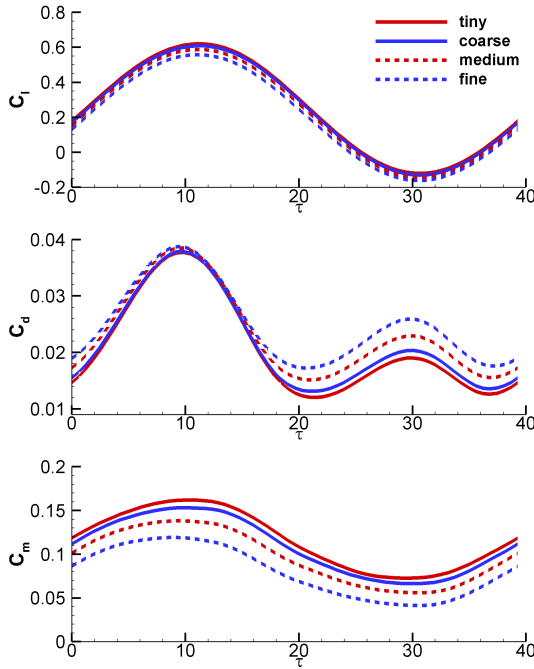
Fig. 3 Spatial grid refinement study of the NASA CRM Case A, using 64 time–intervals per period ($M_\infty = 0.85$, $T_\infty = 311$ K, $Re = 5.0$ million, $k = 0.08$, $\alpha_0 = 0$ deg, $\alpha_A = 3$ deg).

To simulate the sinusoidal motion, the grids undergo a rigid–body motion without deformation. In order to assess the sensitivity of the TD solutions on the level of spatial refinement, Case A was simulated using the four grid levels. In order to assess the sensitivity of the turbulent solutions on the level of temporal refinement, Case A was simulated with the tiny grid using 32, 64 and 128 time–intervals per period. All four TD simulations were run until the maximum values of C_l, C_d and C_m over two consecutive oscillation cycles was less than 0.1%. The number of oscillatory cycles needed to reach this threshold varied between five and seven depending on the spatial and temporal refinements.

Time refinement analysis showed that the computed solution is fairly independent of the number of intervals per period provided that at least 64 time–intervals per period are used. Based on this observation, 64 time–intervals per period were used for the spatial refinement analysis. Figure 3 depicts periodic profiles of C_l, C_d and C_m with the tiny, coarse, medium and fine grids. It is seen that differences exist among all four solutions, indicating that the solution computed with the medium grid is not grid–independent, the same may hold for the solution computed with the fine grid. Due to this fact, and to keep computational cost of the time–dependent analyses within the size of the available resources, medium grid has been used for all further TD and HB analyses.
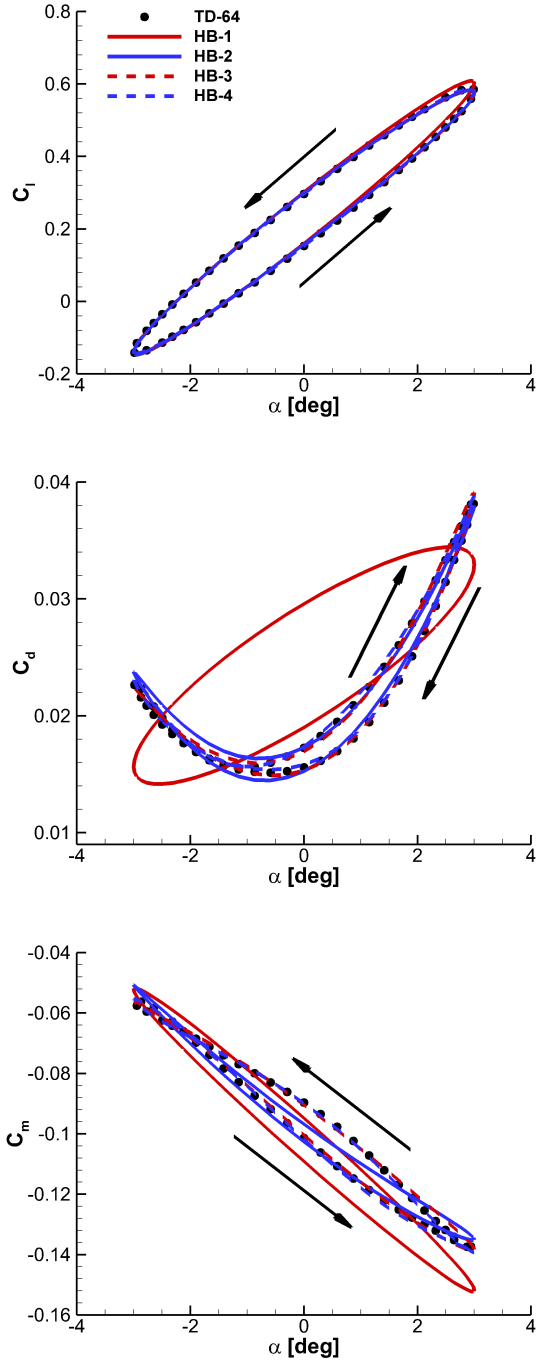
5.2.2 Aerodynamic analysis

To demonstrate the solution accuracy of the HB method, the unsteady solution cases were run using up to four complex harmonics. Figure 4 shows the hysteresis loops of the integrated loads against the instantaneous angle–of–attack. The time evolution of C_l was observed to be nearly linear and harmonic with the forced variation in the motion variable, thus, even one complex harmonic is sufficient to correctly predict the C_l behavior. Since the C_d is quadratic to C_l, at least two harmonics are required to reproduce the shape of C_d, and three harmonics perfectly reproduce the TD simulation result. The same holds for C_m, where three harmonics are sufficient to overlap the TD results.

5.2.3 Dynamic derivatives

This section reports the dynamic derivatives of the NASA CRM case A. The formulation of dynamic derivatives is defined in [3].

Table 1 summarizes the dynamic derivatives, in-phase component of the lift force coefficient $\overline{C}_{l_\alpha}$, the lift force damping coefficient $\overline{C}_{l_q}$, in-phase component of the drag force coefficient $\overline{C}_{d_\alpha}$, the drag force damping coefficient $\overline{C}_{d_q}$, in-phase component of the pitching moment coefficient $\overline{C}_{m_\alpha}$, the pitching moment damping coefficient $\overline{C}_{m_q}$. Frequency-domain results are in good agreement with the respective time-domain results. The table suggests that for the $\overline{C}_{l_\alpha}$ and $\overline{C}_{l_q}$, even one harmonic predicts well the dynamic

Table 1 Dynamic derivatives of the NASA CRM case A.

set-up	$\overline{C}_{l_\alpha}$	$\overline{C}_{l_q}$	$\overline{C}_{d_\alpha}$	$\overline{C}_{d_q}$	$\overline{C}_{m_\alpha}$	$\overline{C}_{m_q}$
HB-1	7.04	-17.00	0.16	-1.27	-0.94	-1.72
HB-2	6.78	-17.01	0.00	-1.75	-0.80	-0.73
HB-3	6.78	-17.30	0.15	0.15	-0.80	-1.00
HB-4	6.81	-17.16	0.15	0.16	-0.81	-0.93
TD-64	6.80	-17.36	0.15	0.16	-0.80	-0.92

5.2.4 Computational performance of the HB solver

Table 2 *HB* speed–up for the NASA CRM case A.

	HB 1	HB 2	HB 3	HB 4	TD-64
speed-up	19.5	11.3	4.1	2.6	1.0

Table 2 reports the *HB speed–up* parameter, defined as the ratio of the runtime of the $TD-64$ simulation and the *HB* analysis with N_H harmonics, and shows that the *HB*2 simulation, which successfully predicts all dynamic derivatives, reduces the analysis runtime by a factor 11.3.
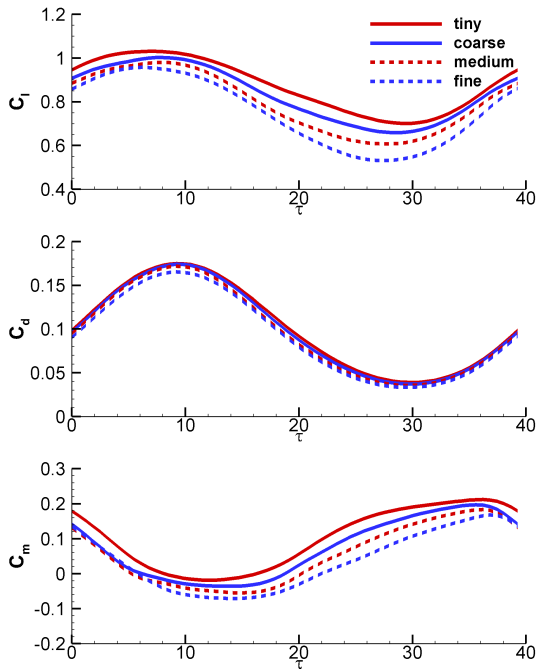
5.3 Forced sinusoidal motion–case B

Case B was selected to represent a complex, unsteady flow problem. Harmonic oscillations are performed at a mean angle of attack above which the lift coefficient becomes nonlinear. The flow conditions are ideal to test the robustness of the *HB* approach in conjunction with the computational speedup to provide admissible results for flight simulation.

5.3.1 Numerical set–up

The reduced frequency is $k = 0.08$, the mean angle of attack is $\alpha_0 = 6$ deg and the amplitude is $\alpha_A = 3$ deg.

The sensitivity of the TD solutions on the level of spatial refinement for Case B was investi-

Fig. 4 Lift coefficient dependence on forced sinusoidal motion of the NASA CRM Case A ($M_\infty = 0.85$, $T_\infty = 311$ K, $Re = 5.0$ million, $k = 0.08$, $\alpha_0 = 0$ deg, $\alpha_A = 3$ deg).

derivatives, whereas for other derivatives, at least two harmonics are required.

Fig. 5 Spatial grid refinement study of the NASA CRM case B ($M_\infty = 0.85$, $T_\infty = 311$ K, $Re = 5.0$ million, $k = 0.08$, $\alpha_0 = 6$ deg, $\alpha_A = 3$ deg).

gated with four grid levels. The sensitivity of the TD solutions on the level of temporal refinement was simulated with the tiny grid using 32, 64 and 128 time–intervals per period. As for Case A, it was found that at least 64 time–intervals per period are necessary. Figure 5 shows periodic time histories of C_l, C_d and C_m for the tiny, coarse, medium and fine grids using 64 time–intervals.

5.3.2 *Aerodynamic analysis*

Figure 6 shows the hysteresis loops for Case B. One notes that there is a significant nonlinearity that distorts the loops. To match the time history values, one harmonic is insufficient at this operating regime. One my notice that at least two harmonics are required to match the TD and HB loops for C_l and C_d, whereas minimum three harmonics are required for the C_m.

Figure 7 depicts the surface pressure coefficient C_p for $\alpha(t) = 6$ deg, for both the upstroke and downstroke movements. It can be seen that the position of the shock is significantly different for two positions with the same $\alpha(t)$, which
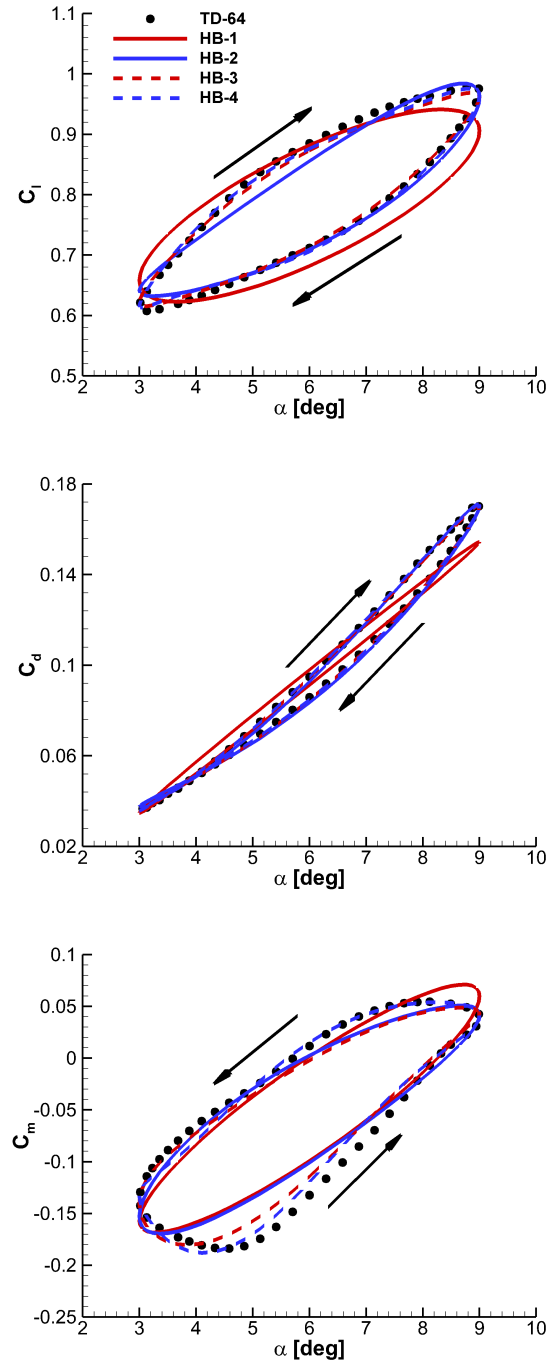
Fig. 6 Lift coefficient dependence on forced sinusoidal motion of the NASA CRM Case B ($M_\infty = 0.85$, $T_\infty = 311$ K, $Re = 5.0$ million, $k = 0.08$, $\alpha_0 = 6$ deg, $\alpha_A = 3$ deg).

demonstrates a complexity of this flow problem.
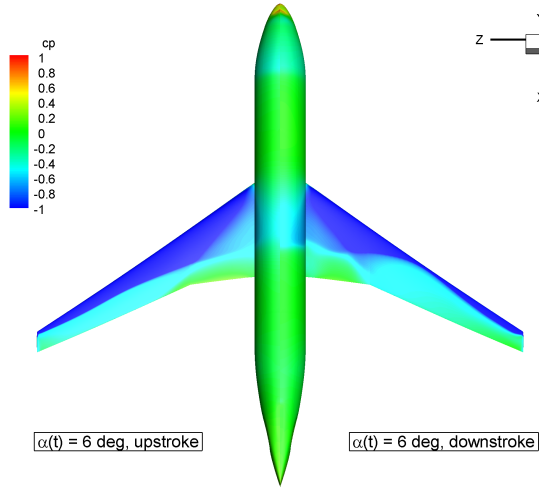
Fig. 7 Surface pressure coefficient plot of the NASA CRM Case B computed with TD–64 ($M_\infty = 0.85$, $T_\infty = 311$ K, $Re = 5.0$ million, $k = 0.08$, $\alpha_0 = 6$ deg, $\alpha_A = 3$ deg).

5.3.3 Dynamic derivatives

This section reports the dynamic derivatives of the NASA CRM case B. The formulation of dynamic derivatives is defined in [3].

Table 3 Dynamic derivatives of the NASA CRM case B.

set-up	$\overline{C}_{l_\alpha}$	$\overline{C}_{l_q}$	$\overline{C}_{d_\alpha}$	$\overline{C}_{d_q}$	$\overline{C}_{m_\alpha}$	$\overline{C}_{m_q}$
HB-1	2.35	24.02	1.13	0.82	2.06	-12.11
HB-2	3.04	17.49	1.26	1.05	1.84	-12.41
HB-3	3.11	17.57	1.27	1.05	1.89	-13.17
HB-4	3.11	18.80	1.27	1.13	1.91	-14.86
TD-64	3.25	19.52	1.28	0.99	1.83	-16.22

Table 3 reports the dynamic derivatives for case B. It can be observed that except for the $\overline{C}_{m_q}$, only two harmonics are required for predictions of the dynamic derivatives.

5.3.4 Computational performance of the HB solver

Table 4 reports the *HB speed–up* parameter, defined as the ratio of the runtime of the $TD - 64$

Table 4 *HB* speed–up for the NASA CRM case B.

	HB 1	HB 2	HB 3	HB 4	TD-64
speed-up	19.5	9.5	5.1	3.5	1.0

simulation and the *HB* analysis with N_H harmonics, and shows that the *HB*2 simulation, which is already sufficiently accurate for the prediction of dynamic derivatives, reduces the analysis runtime by a factor 9.5.

6   Conclusions

A harmonic balance Navier–Stokes approach to the analysis of the NASA common research model periodic flows using the shear stress transport turbulence model has been presented, with particular emphasis on application side, for calculation of dynamic derivatives. The predictive capabilities of the underlying steady code have been validated using steady flow regimes of the NASA common research model experiment. The computational efficiency of the *HB* solver has been assessed by two forced sinusoidal motion cases of the NASA common research model, and it has been shown that the *HB* NS CFD method can reduce the runtime of periodic flow simulations to predict dynamic derivatives by up to 11.3 times over the standard TD method. This acceleration occurs because *HB* method does not require the solution of lengthy transients occurring in TD simulations before achieving the sought periodic state. This achievement is believed to bring the use of NS CFD closer to the calculation of dynamic derivatives for aircraft flight simulation.

References

[1] Allerton D J. Flight simulation – past, present and future. *The Aeronautical Journal*, Vol. 104, No. 1042, pp 651-663, 2000.

[2] Bryan G H. *Stability in Aviation*. MacMillan, London, 1911.

[3] Da Ronch A, McCracken A J, Badcock K J, Widhalm M and Campobasso M S. Linear Fre-

JERNEJ DROFELNIK[*] , ANDREA DA RONCH[*] , M. SERGIO CAMPOBASSO[**]

quency Domain and Harmonic Balance Predictions of Dynamic Derivatives. *Journal of Aircraft*, Vol. 50, No. 3, pp 694-707, 2013.

[4] Hall K C, Thomas J P and Clark W S. Computations of Unsteady Nonlinear Flows in Cascades Using a Harmonic Balance Technique, *AIAA Journal*, Vol. 40, No. 5, pp 879-886, 2002.

[5] Sicot F, Puigt G and Montagnac M. Block-Jacobi Implicit Algorithms for the Time Spectral Method, *AIAA Journal*, Vol. 46, No. 12, pp. 3080-3089, 2008.

[6] Woodgate M A and Badcock K J. Implicit Harmonic Balance Solver for Transonic Flows with Forced Motions, *AIAA Journal*, Vol. 47, No. 4, pp. 893-901, 2009.

[7] Thomas J, Dowell E, Hall K and Denegri C. Modeling Limit Cycle Oscillation Behavior of the F-16 Fighter Using a Harmonic Balance Approach, *45th AIAA/ASME/ASCE/AHS/ASC Structures, Structural Dynamics & Materials Conference, Palm Springs, California, AIAA 2004–1696, 2004.*

[8] Hassan D and Sicot F. A Time–Domain Harmonic Balance Method for Dynamic Derivatives Predictions, *49th AIAA Aerospace Sciences Meeting including the New Horizons Forum and Aerospace Exposition*, Orlando, Florida, AIAA 2011–1242, 2011.

[9] Campobasso M S and Baba-Ahmadi M H. Analysis of Unsteady Flows Past Horizontal Axis Wind Turbine Airfoils Based on Harmonic Balance Compressible Navier-Stokes Equations with Low-Speed Preconditioning. *Journal of Turbomachinery*, Vol. 134, No. 6, 2012.

[10] Campobasso M S, Drofelnik J, Gigante F. Comparative assessment of the harmonic balance Navier-Stokes technology for horizontal and vertical axis wind turbine aerodynamics. *Computers & Fluids* , Vol. 136, pp. 354 - 370, 2016.

[11] Vassberg J, Dehaan M, Rivers M and Wahls R. Development of a Common Research Model for Applied CFD Validation Studies. *26th AIAA Applied Aerodynamics Conference*, Honolulu, Hawaii, AIAA 2008–6919, 2008.

[12] Drofelnik J and Campobasso M S. Comparative turbulent three-dimensional Navier-Stokes hydrodynamic analysis and performance assessment of oscillating wings for renewable energy applications. *International Journal of Marine Energy*, Vol. 16, pp 100 - 115, 2016.

[13] Drofelnik J, Da Ronch A and Campobasso M S. Harmonic balance Navier–Stokes aerodynamic analysis of horizontal axis wind turbines in yawed wind. *Wind Energy*, Vol. 21, No. 7, pp. 515-530, 2018.

[14] Campobasso M S, Piskopakis A, Drofelnik J and Jackson A. Turbulent Navier-Stokes Analysis of an Oscillating Wing in a Power-Extraction Regime Using the Shear Stress Transport Turbulence Model, *Computers and Fluids*, Vol. 88, pp. 136-155, 2013.

[15] Harten A, Lax P D and van Leer B. On Upstream Differencing and Godunov–Type Schemes for Hyperbolic Conservation Laws. *SIAM Review*, Vol. 25, No. 1, pp 35-61, 1983.

[16] 5th AIAA CFD Drag Prediction Workshop, available from: https://aiaa-dpw.larc.nasa.gov/Workshop5/workshop5.html [accessed 13/03/2018].

[17] NASA Common Research Model, https://commonresearchmodel.larc.nasa.gov/ [accessed 13/03/2018].

[18] Levy D, Laflin K, Vassberg J, Tinoco E, Mani M, Rider B, Brodersen O, Crippa S, Rumsey C, Wahls R, Morrison J, Mavriplis D and Murayama M. Summary of Data from the Fifth CFD Drag Prediction Workshop, *51st AIAA Aerospace Sciences Meeting including the New Horizons Forum and Aerospace Exposition*, AIAA 2013–0046, Grapevine, Texas, 2013.

Contact Author Email Address

For more information please contact: j.drofelnik@soton.ac.uk

Copyright Statement